Trumpet solution from spherical gravitational collapse with puncture gauges

Marcus Thierfelder, Sebastiano Bernuzzi, David Hilditch, and Bernd Brügmann

Theoretical Physics Institute, University of Jena, 07743 Jena, Germany

Luciano Rezzolla

Max-Planck-Institut für Gravitationsphysik, Albert-Einstein-Institut, Golm, Germany

We investigate the stationary end state obtained by evolving a collapsing spherical star with the gauges routinely adopted to study puncture black holes. We compare the end state of the collapse with the trumpet solution found in the evolution of a single wormhole slice and show that the two solutions closely agree. We demonstrate that the agreement is caused by the use of the Gamma-driver shift condition, which allows the matter to fall inwards into a region of spacetime that is not resolved by the numerical grid, and which simultaneously finds the stationary coordinates of the trumpet outside the matter.

I. INTRODUCTION

The possibility of obtaining stable evolutions of relativistic compact objects within the framework of numerical relativity relies crucially on the choice of suitable coordinate gauge conditions. In particular, the well-known *puncture* approach relies on the gauge conditions to deal with explicit coordinate singularities present in the computational domain. These gauge conditions are built upon the "1 + log" lapse condition [1] and the "Gamma-driver" shift condition [2], and allow the coordinate singularity (puncture) to be advected across the grid by the shift [3–7]. Hereafter we will refer to these gauge conditions as the *puncture gauges.*

It has been shown [3,8–12] that, for a single puncture without linear momentum or spin, the wormhole topology of the puncture initial data [13] ceases to be resolved by the mesh in the code. Instead, the mesh approaches an asymptotically cylindrical stationary, solution, i.e., the *trumpet* solution. The puncture gauges can thus be viewed as a sort of "natural excision" which squeezes the singularity into an unresolved region of the computational domain. It is nowadays commonly used in binary black-hole simulations by many groups following [6,7].

The puncture gauges have furthermore been tested in a number of codes solving also the equations of relativistic hydrodynamics [14–19]. It has been found effective in handling the black hole that forms in the collapse of a neutron star [15,20,21], and in binary systems in general (see, e.g., [16,17,19,22,23] and references therein). In [15], in particular, it was first shown with three-dimensional (3D) simulations that when using the puncture gauges no special treatment beyond standard artificial dissipation for the metric variables is necessary to follow stably the black-hole formation and evolution.

In this paper we show that the numerical evolution, with the puncture gauge, of a collapsing spherical star approaches the trumpet solution at late times. This result is not trivial for a number of reasons. First, because in the collapsing spacetime, and, in particular, in the portion filled by matter, there is no timelike Killing vector and it is not clear how a stationary end state can be found. Second, at the continuum level, the two spacetimes are clearly different since, for example, slices in the two foliations have a different topology. Even restricting our attention to the vacuum region of the collapsing spacetime and assuming a Killing slice compatible with the 1 + log lapse condition, it is not obvious that the resulting slice will be exactly that reported in [3]. Finally, the collapsing matter inside the apparent horizon is observed to disappear but it is not clear whether this reflects a physical or a numerical behavior.

We therefore seek answers to the following questions: (i) How well do the two end states agree? (ii) Where does the matter go after the apparent horizon is formed? (iii) How do the gauges find a stationary slicing of a spacetime without an explicit timelike Killing vector? In order to address these questions we evolve the spacetime of a star collapsing to a black hole using a 1 + log slicing condition and two variants of the Gamma-driver shift condition. The different results are then compared *quantitatively* with the trumpet solution, and spacetime diagrams are constructed to follow the motion of the matter. Overall we find that the two spacetimes tend to a common stationary solution at late times and that this agreement is primarily caused by the shift condition, which pushes grid points away from regions of high curvature, preventing the matter from being resolved on the numerical mesh.

The plan of the paper is as follows. In Sec. II we briefly review our numerical methods, presenting the numerical results and their interpretation in Sec. III. Our conclusions are summarized in Sec. IV, while we dedicate the Appendix to a description of our method for constructing spacetime diagrams for spherical spacetimes.

II. NUMERICAL SETUP

We perform numerical simulations both in explicit spherical symmetry by means of the one-dimensional (1D) code described in [24] and in 3D by means of BAMMATTER [25]. The latter is developed extending the hydrodynamics solver of the spherical code into the BAM code [26]. More specifically, we solve the full set of Einstein equations in the $3 + 1$ formalism coupled to general relativistic hydrodynamics (GRHD). In our spherically symmetric simulations we adopt both the BSSNOK and Z4c formulations of the Einstein field equations (see [24] for details), while in 3D we use only the BSSNOK formulation.

As mentioned above, our gauges are built upon the $1 +$ log condition [1] for the lapse α and the Gamma-driver condition for the shift β^i [2] written in the form

$$\partial_t \alpha = \beta^i \alpha_{,i} - \alpha^2 \mu_L \hat{K}, \tag{1}$$

$$\partial_t \beta^i = \mu_S \tilde{\Gamma}^i - \eta \beta^i + \beta^j \beta^i_{,j}, \tag{2}$$

where we always choose $\mu_L = 2/\alpha$, with either $\mu_S = 1$ or $\mu_S = \alpha^2$ and $\eta = 2/M$. The Gamma-driver condition (2) may be obtained as the first integral of what is implemented in most numerical-relativity codes. A comparison of the behavior of the condition (2) with the standard form in the evolution of puncture black holes is presented in [4].

For the evolution of the matter we adopt the Valencia flux-conservative formulation of the equations of GRHD [27–29] for a perfect fluid. A property of flux-conservative formulations is that they preserve (exactly in the continuum) certain integral quantities such as the total rest mass of the fluid, M_0, or its momentum and energy density. The equations of state employed to describe the fluid are the ideal-gas or the polytropic equations of state [28]: no significant differences were found when using one or the other.

In both codes the numerical evolution in time relies on the method-of-lines with Runge-Kutta integrators and finite difference approximations. The GRHD equations are solved by means of a high-resolution shock-capturing scheme based on the local Lax-Friedrich central scheme [30] combined with convex essentially nonoscillatory [31] reconstruction [24,25].

In analogy with [15] and in contrast to [24], we do not find it necessary to excise the hydrodynamical variables in the collapse evolutions. Artificial Kreiss-Oliger dissipation is added in the evolution of the metric fields following the standard procedure [26]. Instead, we find it important to set the GRHD eigenvalues to zero if unphysical values are computed ("eigenvalue excision"). Note that this is compatible with the use of the local Lax-Friedrich central scheme, which requires only an estimate of the local speed. Unphysical values can be produced in a neighborhood of the center of the collapse, due to numerical errors.

In 3D simulations we also found it important to set a ceiling on the Lorentz factor W in order to prevent the code from crashing after the formation of the apparent horizon. In particular W is set to the ceiling value $W_{\text{ceil}} = 10^{10}$ when (and only when) the velocity becomes larger than the speed of light. Simulations employing the excision of the hydrodynamical quantities were also performed. In this case, the matter variables are set to the atmosphere value in a small region well inside the apparent horizon. As expected, no differences were found. In the following we focus on simulations without excision.

The initial stellar model is an unstable spherical configuration widely used in the literature, e.g., [28]. Adopting units in which $c = G = M_\odot = 1$, the configuration chosen has central rest-mass density $\rho_c = 7.993 \times 10^{-3}$, gravitational (ADM) mass $M = 1.448$ ($M_0 = 1.535$) and circumferential radius $R = 5.838$ (isotropic coordinate radius $r_R = 4.268$). The collapse is triggered imposing a negative velocity perturbation which is larger than the truncation error [28]. For the vacuum simulations we use standard puncture data [13] in isotropic coordinates and with an ADM mass, which is the same as that of the star.

The simulations in 1D were performed on a grid with uniform spacing with resolutions $\Delta_r = 0.02, 0.01, 0.005$. The simulations in 3D, on the other hand, were performed imposing an octant symmetry on a cell-centered Cartesian grid with 8 fixed mesh refinement levels, with the resolutions of finest level given by $\Delta_{xyz} = 0.05, 0.03125, 0.025$, and where the resolution doubles from one level to the next.

III. RESULTS

We next describe the results of the different numerical simulations. Before that, however, it is useful to recall some of the basic properties of the evolutions that from the puncture spacetime lead to the trumpet solution or that from a stellar spacetime lead to a black-hole solution.

Puncture spacetime.—The evolution of the puncture spacetime is described in Ref. [3,11]. The initial Schwarzschild slice in the isotropic coordinate evolves, driven by the puncture gauges, to the stationary trumpet solution. Approximate stationarity is achieved within an evolution time of about $60M$, depending on the details of the gauge choice. Asymptotically, there is a coordinate singularity at the puncture point at $r = 0$, which corresponds to a sphere with Schwarzschild radius $R_0 \approx 1.3M$. The trumpet slice extends from R_0 to spatial infinity, i^0, while the wormhole slice of the initial data reaches from the outer i^0 to an inner spatial infinity. Conceptually, it is important to distinguish between the analytical solution and the numerical solution on a discrete grid, and also between the wormhole slice of the analytical evolution and the trumpet slice which is only reached asymptotically. The evolution starts with a wormhole slice which, due to the continuity of the analytical solution, remains a

wormhole slice. It asymptotes to a trumpet slice in the sense that the region inside R_0 has a coordinate size that tends toward zero. Numerically, this inner region is effectively excised once its coordinate size drops below the grid spacing. Assuming that there is no grid point at the puncture itself, after a short evolution time the numerical grid only has grid points outside R_0, that is, only the trumpet part of the initial wormhole is represented. Anticipating the discussion of matter, the key difference is that the initial data with matter lives neither on a wormhole nor a trumpet slice, since the matter "covers" the inner region of the slice.

Collapsing spacetime.—The dynamics of a collapsing unstable star in general relativity has been discussed in great detail in a number of papers and we refer the interested reader to Refs. [15,28,29] for some of the most recent work. For the test case considered here ($\mu_S = 1$), the introduction of the perturbation is sufficient to drive the star over the stability threshold and induce its gravitational collapse. As a result, matter essentially freely falls toward the center, leading to an exponential growth of the rest-mass density and a related rapid variation of the metric functions. This is shown in the top panel of Fig. 1, which exhibits the radial profile of the rest-mass density at some representative times. The "singularity-avoiding" properties of the $1 + \log$ slicing condition drive the lapse function to very small values near the origin. This is shown in the middle panel of Fig. 1, while the bottom one refers to the
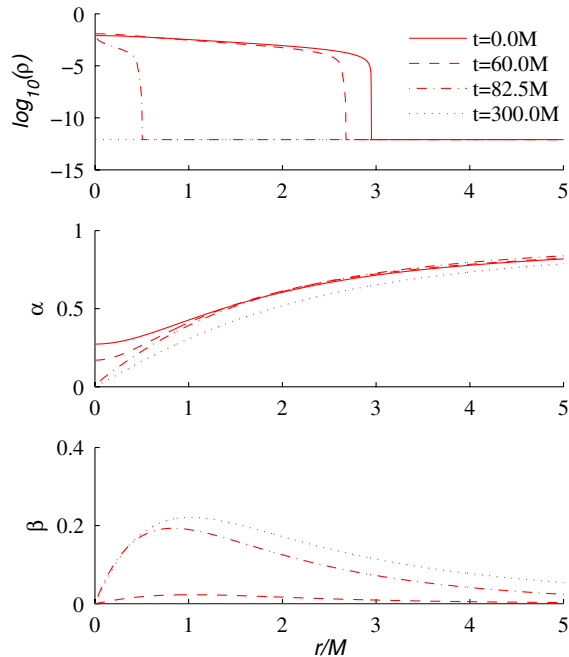

FIG. 1 (color online).   Radial profiles of the rest-mass density ρ (top panel), of the lapse function α (middle panel), and of the shift $\beta \equiv \beta^r$ (bottom panel) at some representative times of the evolution. Note that at $t \sim 50M$ an apparent horizon is first found and that by $t = 300M$ the amount of matter on the final time slice is essentially that in the atmosphere.

evolution of the shift. Note that as the matter rushes toward the center, the shift still succeeds in arresting the motion of the radial coordinates outside the matter distribution (ignoring the atmosphere), thereby preventing slice stretching (in the sense of stretching of the spatial coordinates) as for the black-hole evolutions. At about $t \sim 50M$, an apparent horizon forms indicating unambiguously the presence of a black hole. This time represents the time when a first comparison between the two spacetimes can, in principle, be made. We also note that because the coordinate radius of the apparent horizon is initially $r_{AH} \lesssim 2M$, part of the matter is outside of it, but it is then rapidly accreted.

As highlighted in [15], the gauge conditions in Eqs. (1) and (2) allow us to follow the subsequent evolution without having to excise either the hydrodynamical or the gravitational field variable. The conservation of the rest mass is very good up to the horizon formation: $\Delta M_0(t)/M_0(0) \lesssim 0.05\%$. After the formation of the apparent horizon, the matter inside is observed to disappear from the numerical grid, so that by $t = 300M$ the amount of matter on the slice is that in the atmosphere, $M_0(300) \sim 10^{-6}M_0(0)$. As we will discuss in Sec. III B, a suitable change in the value of μ_S for the shift condition can avoid this behavior.

As a side remark we note that in our 1D simulations we observe a better behavior of the Z4c formulation of the Einstein equation with respect to the BSSNOK one in terms of constraint violation and long-term stability. In particular, at $t = 2500M$, the L2 norm of the Hamiltonian constraint is about 4 orders of magnitude lower with Z4c. Furthermore, at $t = 2500M$, the irreducible mass of the final black hole in the Z4c evolutions is within the numerical error of the ADM mass of the initial data. In contrast, the BSSNOK simulations display a significant deviation in the irreducible mass of the black hole after $t = 300M$. In view of this, in what follows, the 1D results we will present refer exclusively to those obtained for the Z4c formulation.

A. Agreement of the end-states

In this section we investigate the asymptotic slice reached at the end of the evolution by the collapsing star and compare it with the corresponding trumpet one. This is shown in Fig. 2, which reports several metric fields at time $t = 300M$. This time is well after the apparent horizon is first found (i.e., $t_{AH} \sim 50M$), and represents in both cases a time when the solution has become essentially stationary. From top to bottom the different panels refer, respectively, to: the trace of extrinsic curvature (K), the conformal factor (χ), the lapse (α), and the shift (β^r). It is quite apparent that at the selected time the two spacetimes are extremely similar and it is difficult to distinguish the solutions by a visual inspection.

To obtain a more quantitative estimate of the differences we have computed the behavior of the fields in the collapsing spacetime near the origin and obtained the following fitting functions for the stationary solution for $r \ll 1$:
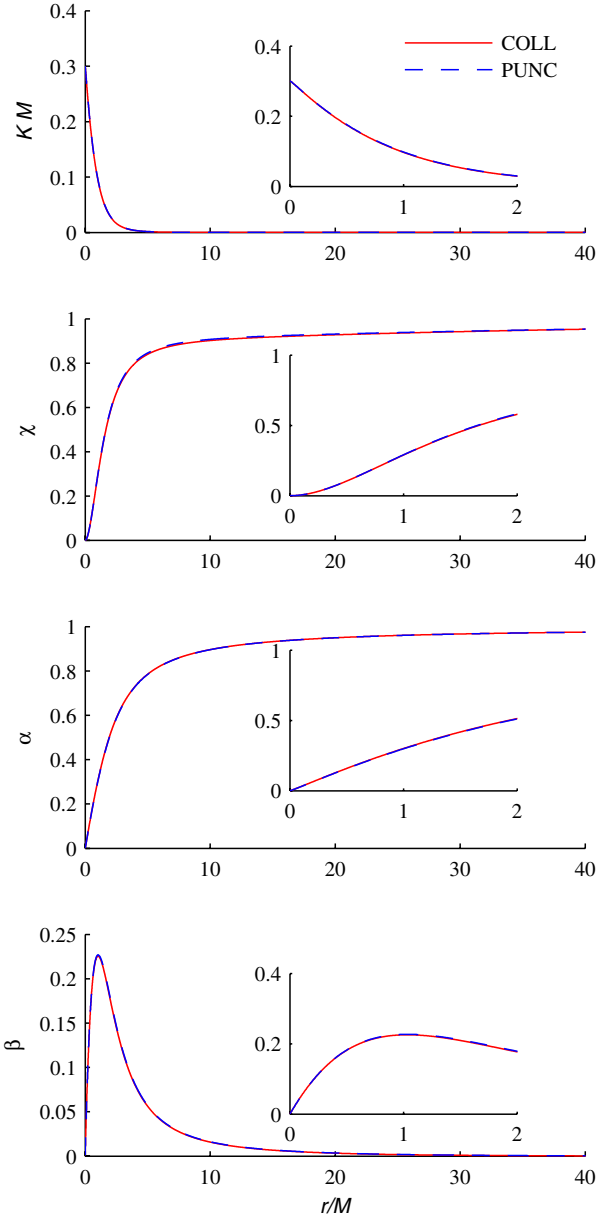
FIG. 2 (color online). Radial profiles of representative field variables at time $t = 300M$ from the 1D simulations of the puncture and the collapsing star. From top to bottom: trace of extrinsic curvature (K), conformal factor (χ), lapse (α), and shift ($\beta \equiv \beta^r$).

$$KM \sim 0.30 - 0.37\left(\frac{r}{M}\right), \quad (3)$$

$$\chi \sim 1.22\left(\frac{r}{M}\right)^{2.0}, \quad (4)$$

$$\alpha \sim 0.54\left(\frac{r}{M}\right)^{1.09}. \quad (5)$$

The fits for (4) and (5) contain the exponent of r as a fitting parameter, but not for (3). The result agrees well with the

corresponding expressions in [32]. In particular, the non-integer exponent for the lapse in (5) is very close to the analytic expression for the trumpet solution in isotropic coordinates, which has exponent 1.091 [32]. This is interesting since the numerical coordinates are not isotropic, although one could argue that close to the puncture the isotropy of the initial data is maintained during the evolution.

This result is confirmed when considered also in a coordinate-independent manner. Following the prescription suggested in [3], we analyze the dependence of the lapse versus the extrinsic curvature and report in Fig. 3 the differences at different times. More specifically, we show with solid lines the relative difference $\Delta\alpha/\alpha \equiv \alpha_{punc}/\alpha_{coll} - 1$, between the lapse of the puncture evolution, α_{punc}, and that of the collapsing star, α_{coll}, either when the apparent horizon has just formed ($t \sim 50M$) or when the solutions have reached a stationary stage ($t \sim 300M$).

It is clear that the relative difference decreases in time and, at time $t = 300M$, it is below 0.1%. By performing convergence tests we have also determined that the numerical errors are at the same level as the 0.1% disagreement. Also reported in Fig. 3, with dashed lines, is the relative difference between the puncture data and the analytic solution for the trumpet solution [11,32]

$$K = \beta\alpha'(R)/2$$

$$= \frac{\sqrt{2/R(\alpha) + \alpha^2 - 1}(4R(\alpha)\alpha^2 - 4R(\alpha) + 6)}{2R(\alpha)(R(\alpha)\alpha^2 - 2R(\alpha)\alpha - R(\alpha) + 2)}, \quad (6)$$
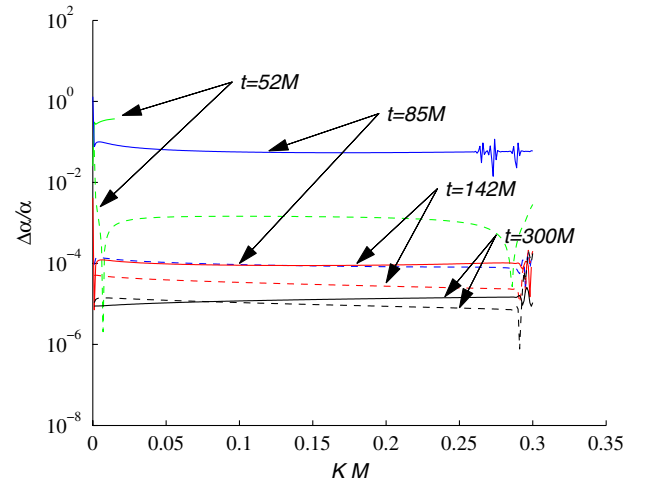

FIG. 3 (color online). Relative difference $\Delta\alpha/\alpha \equiv \alpha_{punc}/\alpha_{coll} - 1$, between the lapse of the puncture evolution, α_{punc}, and that of the collapsing star, α_{coll}, as a function of the trace of the extrinsic curvature, K, at different coordinate times. For a fair comparison, data at the same K are found by interpolation. The dashed lines refer to the relative differences between the analytic result and the puncture evolution. By construction, for early times this difference is much smaller than the difference between puncture and matter simulations.
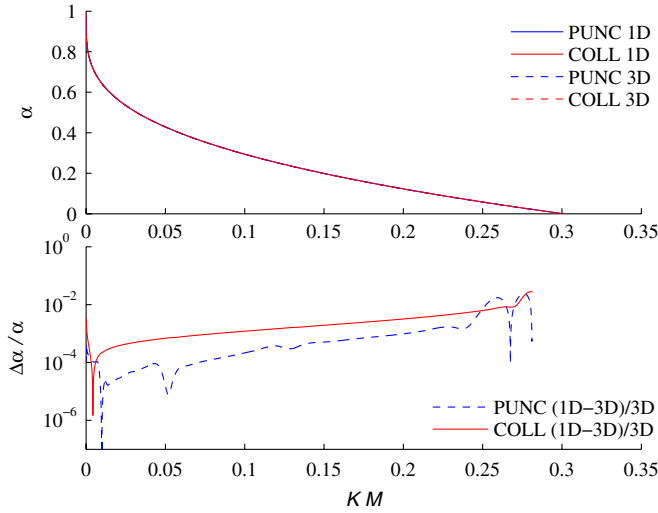
FIG. 4 (color online). Slicing from 1D and 3D simulations. Top panel: the lapse (α) is plotted versus the trace of the extrinsic curvature K at time $t = 300M$ for the collapse in 1D (red solid line) and the puncture evolution (blue solid line) spacetimes, and the collapse in 3D (red dashed line) and collapse (blue dashed line) spacetimes. Bottom panel: relative differences. Note that 1D results, computed on a finer grid, are interpolated for the comparison.

where R is the Schwarzschild radius, α' is the derivative of α with respect to R, and we set $M = 1$. As expected, the relative difference is, in this case, much smaller initially, but it becomes comparable with the one computed for the collapsing spacetime at later times.

It is possible to model the behavior of the data from the collapsing spacetime near the origin and at $t = 300M$ as

$$KM \sim 0.30 - 0.92\alpha. \qquad (7)$$

Similarly, a Taylor expansion of Eq. (6) around $\alpha = 0$ (i.e., for the values of the lapse near the puncture) can be performed by using the implicit function $R(\alpha)$ in [32], yielding

$$K(\alpha) = 0.300\,937 - 0.930\,916\alpha + O(\alpha^2), \qquad (8)$$

which closely agrees with Eq. (7).

Finally, we note that we did not find significant differences between the 1D and the 3D results for the collapsing spacetime. This is summarized in Fig. 4, where the top panel shows α versus K for the 1D and the 3D data at time $t = 300M$: they are visually indistinguishable. Similarly, the bottom panel shows that the relative differences between the 1D and the 3D data are generically below 2%.

B. Where does the matter go once inside the horizon?

As discussed above, the numerical evidence obtained when using the Gamma-driver shift condition with $\mu_S = 1$ is that the matter inside the apparent horizon is progressively "dissipated" (see also [15] where this was first discussed). This behavior is clearly displayed in the upper panel of Fig. 5, in which the total rest mass normalized to
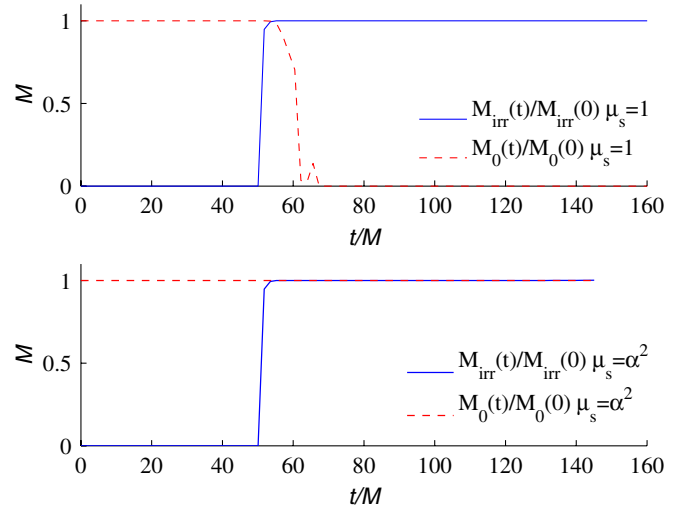

FIG. 5 (color online). Evolution of the total rest mass, $M_0(t)$, (red dashed lines) and of the irreducible mass, $M_{irr}(t)$, (blue solid lines) normalized, respectively, to the initial value and to the ADM mass. The top panel refers to a simulation with gauge speed $\mu_s = 1$, and the bottom panel to evolutions with gauge speed $\mu_s = \alpha^2$.

the initial value is plotted in time (dashed red line). Note that at about $10M$ after the formation of the apparent horizon the normalized rest mass drops smoothly to zero except for a small bump near $t = 65M$ generated by numerical errors inside the horizon. Also shown is the irreducible mass of the black hole normalized to the ADM mass (solid blue line), which is obviously zero before the apparent horizon is found. This behavior may appear puzzling since it is geometrically clear that the matter cannot leave the foliation (see, e.g., Fig. 6.11 of [33]). In addition, since we are using high-resolution shock-capturing schemes, our numerical methods should be sufficiently robust, for reasonable spatial resolutions, to handle extremely large gradients as the matter piles up in the collapse. Indeed, we have experimented with various reconstruction algorithms and resolutions and found that both affect slightly the rate and the initial time of the disappearance of the fluid. More specifically, more dissipative schemes result in an earlier disappearance of the matter, while higher resolutions can delay it. However, neither improvement prevents the disappearance of the matter from the grid.

In order to establish whether this behavior is instead due to an excessive stretching of the spatial coordinates generated by the Gamma-driver shift condition, we have performed the same simulations using either a shift gauge speed $\mu_S = \alpha^2$, or simply setting $\beta^i = 0$. We recall that this is possible since the $1 + \log$ lapse condition is a pure slicing condition, so that the foliation is unaffected by a change of radial gauge (see, for example, [10,34]).

The results of these tests are shown in the bottom panel of Fig. 5, where we report with the evolution of the total rest-mass (dashed red lines) and of the normalized

irreducible mass (solid blue lines) when $\mu_S = \alpha^2$. Clearly, while the behavior of the irreducible mass is independent of the choice for μ_S, that of the rest mass is not. When using the $\mu_S = \alpha^2$ radial gauge, in fact, the matter remains on the numerical grid, so that the rest mass is conserved well beyond the formation of the apparent horizon. The cause of this difference must therefore to be attributed to the large stretching of the spatial coordinates with $\mu_S = 1$. Specifically, we identify two effects. First, matter falls inside the innermost grid point as the inner boundary is effectively an outflow boundary for the matter; M_0 starts to drop to the atmosphere value approximately $10M$ before the stellar surface passes through the innermost gridpoint. At this time, the areal radius of the innermost gridpoint grows rapidly to approximately $1.9M$ (see also Fig. 6 later). Second, the effective resolution in areal radius near the time of the stellar surface passing through the innermost gridpoint is approximately an order of magnitude lower than in the initial data. The stretching is thus so large that the matter "percolates" through the grid as the numerical methods are not able to reproduce its steep gradients. As a result, the spacetime "empties" itself and this explains the very good match with the trumpet solution reported in Fig. 3. Conversely, when $\mu_S = \alpha^2$, the radial gauge does not distort the grid significantly, allowing for an excellent conservation of the rest mass on the grid. Note that the latter is not the result of the rather high spatial resolution, but it is simply the result of the coordinate time "freezing" induced by the collapsed lapse function. Of course, because the spacetime is not able to remove its matter content, the match with the trumpet solution is in this case much worse and $\Delta\alpha/\alpha \sim 10^{-1}$ for $KM \gtrsim 0.21$.

Not surprisingly, much of what we discussed so far for $\mu_S = \alpha^2$ applies also when considering $\beta^i = 0$. However, the same dynamics that leads a $\beta^i = 0$ shift condition to fail in a curved spacetime, is responsible for the late-time failure of the simulations having $\mu_S = \alpha^2$ as gauge speed. As a result, a Gamma-driver shift condition with $\mu_S = 1$ appears to be the most robust choice for all those situations in which a compact fluid object may collapse to a black hole.

Finally, we show in Figs. 6 and 7 the spacetime diagrams as built from the numerical data. The axes in Fig. 6 refer to the time and spatial coordinates used, respectively, in the simulations with $\mu_S = 1$ (upper panel) and $\mu_S = \alpha^2$ (bottom panel). The shaded green area corresponds to the region of the spacetime covered by matter, vertical lines are line of constant Schwarzschild radius while horizontal lines are lines of constant coordinate time. The thick red line emerging after $t \sim 50M$ is the apparent horizon. Figure 6 can be compared with other numerically generated diagrams of collapsing spacetimes obtained either in other gauges [35], or with excision techniques [29], or for puncture evolutions of single black holes [11]. The figure clearly shows how the matter is "squeezed" from the
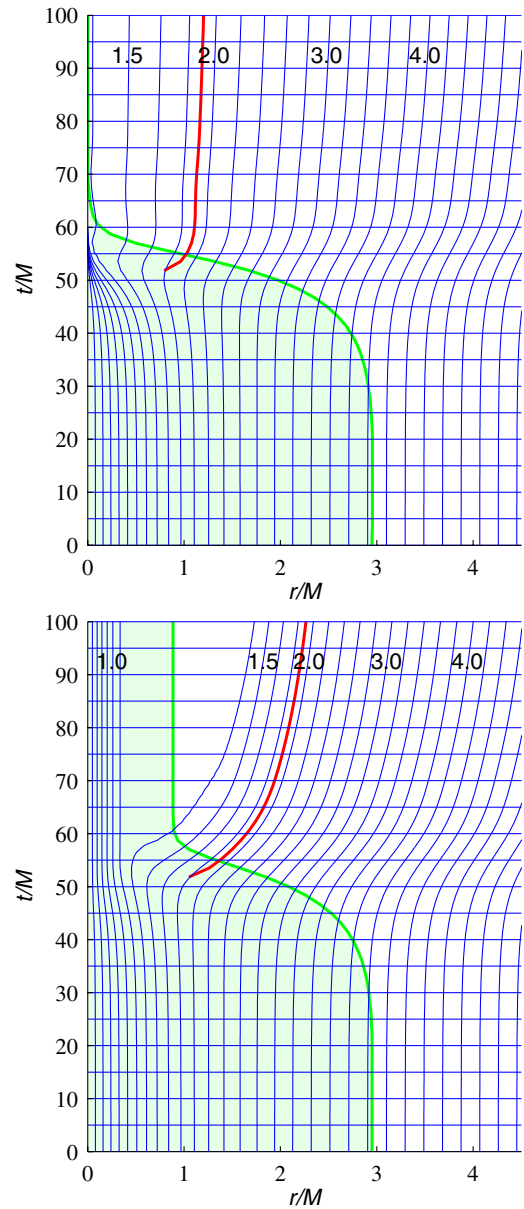

FIG. 6 (color online). Spacetime diagram of the collapsing star. Data are from 1D simulations with gauge speed $\mu_S = 1$ (top panel) and $\mu_S = \alpha^2$ (bottom panel). The horizontal blue lines are lines of constant coordinate time. The thick red line denotes the apparent horizon. The vertical blue lines are lines of constant Schwarzschild radius R which values are on top of the lines. The shaded green area bounded by the thick green lines shows the region of the matter.

numerical grid when $\mu_S = 1$, while it remains on the grid when $\mu_S = \alpha^2$. In both cases an apparent horizon is found. The comparison of the lines of the constant Schwarzschild radius in the two panels highlights the stretching of the spatial coordinate discussed before.

Figure 7 displays the causal spacetime diagram of the collapse. Similarly to Fig. 6 the thick red line denotes the apparent horizon, the thick green line the surface of the collapsing star and the shaded area shows the region
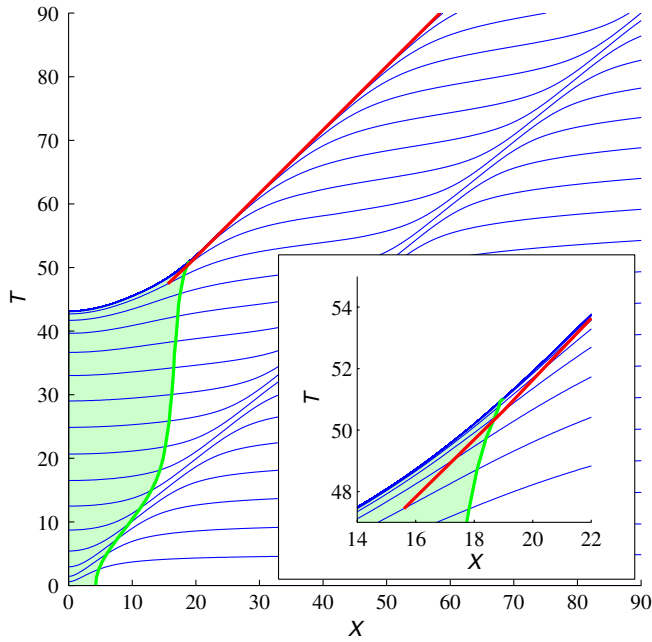
FIG. 7 (color online). Causal spacetime diagram of the collapsing star. Data are from 1D simulations with gauge speed $\mu_S = \alpha^2$. The coordinate axes are constructed so that the light speeds have magnitude one. The horizontal blue lines are lines of constant coordinate time. The thick red line denotes the apparent horizon. The shaded green area bounded by the thick green lines shows the region of the matter.

filled by the matter. The coordinates (X, T) are constructed so that the light speeds have magnitude one, with light cones opening at $45°$ in the diagram. The method employed for the construction is discussed in the Appendix. Because it is easier to use, the data employed to construct the diagram refers to a 1D simulation with $\mu_S = \alpha^2$, but in principle we expect that a very similar diagram would be produced with $\mu_S = 1$. At early times the causal spacetime diagram clearly shows the extremely high speed of the stellar surface and the causal separation between the points initially belonging to the exterior and those that are causally connected to the collapse (see the gauge-wave propagating at the speed of light). At late times it is evident that the collapse of the lapse prevents the slices from evolving forward into the singularity; furthermore, the inset demonstrates that there is always some numerical data inside the horizon.

V. CONCLUSION

By comparing the numerical evolution of a single puncture with that of a collapsing star when using the same puncture gauges, we have shown numerically that the two spacetimes tend to the same trumpet solution at late times, a possibility already conjectured in [15]. Let us explicitly address the questions raised in the Introduction: (i) In the domain covered by the numerical coordinates, at late times, the spacetimes agree within the precision of our

calculations. (ii) The apparently bizarre agreement, which is not possible at the continuum level, is caused primarily by the Gamma-driver shift condition, which stretches the numerical spatial grid. The matter is rapidly forced inside the innermost grid point, preventing it from being resolved and effectively removing it from the spatial slice. Thus, in the domain covered by the numerical coordinates the spacetimes agree, solving the apparent contradiction. (iii) Since the matter is lost inside the innermost gridpoint, at late times, on the numerical grid the evolution is simply that of the vacuum Schwarzschild solution.

We also note that if the matter in the slice is sufficiently compact and in the vacuum region and one has a Killing slicing which is compatible with the "1 + log" gauge, then in the vacuum region the slice must agree with the original "1 + log" trumpet [36]. Our analysis also demonstrates that, while the puncture gauges with $\mu_S = 1$ results in robust numerical evolutions in a collapse scenario, by construction the resulting coordinates are not appropriate for a detailed study of the dynamics of the matter near the singularity.

APPENDIX: THE CONSTRUCTION OF SPACETIME DIAGRAMS

In this appendix we describe our approach to the construction of spacetime diagrams in spherical symmetry. The approach is based on that of [37]. The most general spherical line element can be written as

$$ds^2 = -\alpha^2 dt^2 + \gamma_{rr}(dr + \beta^r dt)^2 + \gamma_{\theta\theta}d\Omega^2, \quad (A1)$$

where $d\Omega^2 = d\theta^2 + \sin^2\theta d\phi^2$ is the standard metric on the two-sphere. The incoming and outgoing radial light speeds are given by

$$c_\pm = -\beta^r \pm \frac{\alpha}{\sqrt{\gamma_{rr}}}. \quad (A2)$$

Ingoing and outgoing null coordinates (u, v) satisfy the equations of motion

$$\partial_t u = -c_+ \partial_r u, \qquad \partial_t v = -c_- \partial_r v, \quad (A3)$$

in coordinates (t, r, θ, ϕ). Assuming that near the outer boundary r_* space is almost flat, we arrive at the boundary condition

$$v(t, r_*) = 2t - u. \quad (A4)$$

We introduce the scalar fields

$$X = \tfrac{1}{2}(v - u), \qquad T = \tfrac{1}{2}(u + v). \qquad (A5)$$

They satisfy the equations of motion

$$\partial_t X = \beta^r \partial_r X + \frac{\alpha}{\sqrt{\gamma_{rr}}} \partial_r T,$$
$$\partial_t T = \beta^r \partial_r T + \frac{\alpha}{\sqrt{\gamma_{rr}}} \partial_r X, \qquad (A6)$$

and are naturally adjusted to the causal structure of the spacetime. In terms of (T, X, θ, ϕ) the spherical line element becomes

$$ds^2 = \psi^4(-dT^2 + dX^2) + \gamma_{\theta\theta}d\Omega^2, \qquad (A7)$$

where ψ^4 is a conformal factor determined by

$$\psi^4 = \frac{\gamma_{rr}}{(\partial_r X)^2 - (\partial_r T)^2}. \qquad (A8)$$

To construct spacetime diagrams we simply evolve the fields (u, v). As initial data we choose $u = -r$ and $v = r$. There are potential problems associated with the breakdown of the coordinate chart, but we will not concern ourselves with those issues here. From our computations we observed, however, that the method requires further development (e.g., a treatment of the fields at the horizon) to construct spacetime diagrams for every numerically generated spacetime (cf. Sec. III B of [11]). In particular we found the construction of causal spacetime diagrams with $\mu_S = 1$ troublesome, perhaps because more sophisticated boundary conditions are required.

[1] C. Bona, J. Masso, E. Seidel, and J. Stela, Phys. Rev. Lett. **75**, 600 (1995).
[2] M. Alcubierre, B. Brügmann, P. Diener, M. Koppitz, D. Pollney, E. Seidel, and R. Takahashi, Phys. Rev. D **67**, 084023 (2003).
[3] M. Hannam, S. Husa, D. Pollney, B. Brügmann, and N. O'Murchadha, Phys. Rev. Lett. **99**, 241102 (2007).
[4] J. R. van Meter, J. G. Baker, M. Koppitz, and D. I. Choi, Phys. Rev. D **73**, 124011 (2006).
[5] D. Pollney, C. Reisswig, L. Rezzolla *et al.*, Phys. Rev. D **76**, 124002 (2007).
[6] J. G. Baker, J. Centrella, D. I. Choi, M. Koppitz, and J. van Meter, Phys. Rev. Lett. **96**, 111102 (2006).
[7] M. Campanelli, C. O. Lousto, P. Marronetti, and Y. Zlochower, Phys. Rev. Lett. **96**, 111101 (2006).
[8] M. Hannam, S. Husa, B. Brügmann, J. A. Gonzalez, U. Sperhake, and N. O. Murchadha, J. Phys. Conf. Ser. **66**, 012047 (2007).
[9] J. D. Brown, Phys. Rev. D **77**, 044018 (2008).
[10] D. Garfinkle, C. Gundlach, and D. Hilditch, Classical Quantum Gravity **25**, 075007 (2008).
[11] M. Hannam, S. Husa, F. Ohme, B. Brügmann, and N. O'Murchadha, Phys. Rev. D **78**, 064020 (2008).
[12] K. A. Dennison, J. P. Wendell, T. W. Baumgarte, and J. D. Brown, Phys. Rev. D **82**, 124057 (2010).
[13] S. Brandt and B. Brügmann, Phys. Rev. Lett. **78**, 3606 (1997).
[14] M. D. Duez, Y. T. Liu, S. L. Shapiro, and B. C. Stephens, Phys. Rev. D **72**, 024028 (2005).
[15] L. Baiotti and L. Rezzolla, Phys. Rev. Lett. **97**, 141101 (2006).
[16] M. Shibata and K. Uryu, Classical Quantum Gravity **24**, S125 (2007).
[17] F. Loffler, L. Rezzolla, and M. Ansorg, Phys. Rev. D **74**, 104018 (2006).
[18] J. A. Faber, T. W. Baumgarte, Z. B. Etienne, S. L. Shapiro, and K. Taniguchi, Phys. Rev. D **76**, 104021 (2007).
[19] L. Baiotti, B. Giacomazzo, and L. Rezzolla, Phys. Rev. D **78**, 084033 (2008).
[20] L. Baiotti, I. Hawke, and L. Rezzolla, Classical Quantum Gravity **24**, S187 (2007).
[21] P. J. Montero, J. A. Font, and M. Shibata, Phys. Rev. D **78**, 064037 (2008).
[22] Z. B. Etienne, J. A. Faber, Y. T. Liu, S. L. Shapiro, K. Taniguchi, and T. W. Baumgarte, Phys. Rev. D **77**, 084002 (2008).
[23] B. Giacomazzo, L. Rezzolla, and L. Baiotti, Mon. Not. R. Astron. Soc. **399**, L164 (2009).
[24] S. Bernuzzi and D. Hilditch, Phys. Rev. D **81**, 084003 (2010).
[25] M. Thierfelder, S. Bernuzzi, and B. Brügmann (unpublished).
[26] B. Brügmann, J. A. Gonzalez, M. Hannam, S. Husa, U. Sperhake, and W. Tichy, Phys. Rev. D **77**, 024027 (2008).
[27] F. Banyuls, J. A. Font, and J. M. A. Ibanez, and J. M. A. Marti, and J. A. Miralles, Astrophys. J. **476**, 221 (1997).
[28] J. A. Font *et al.*, Phys. Rev. D **65**, 084024 (2002).
[29] L. Baiotti *et al.*, Phys. Rev. D **71**, 024035 (2005).
[30] A. Kurganov and E. Tadmor, J. Comput. Phys. **160**, 241 (2000).
[31] X. Liu and S. Osher, J. Comput. Phys. **142**, 304 (1998).
[32] B. Brügmann, Gen. Relativ. Gravit. **41**, 2131 (2009).
[33] R. M. Wald, *General Relativity* (Chicago University Press, Chicago, 1984), p. 491.
[34] M. Alcubierre, Classical Quantum Gravity **20**, 607 (2003).
[35] S. L. Shapiro and S. A. Teukolsky, Astrophys. J. **298**, 34 (1985).
[36] N. O'Murchada (private communication).
[37] N. Ortiz and O. Sarbach, AIP Conf. Proc. **1256**, 349 (2010).